Proceedings of
11th European Conference on Turbomachinery Fluid dynamics & Thermodynamics
ETC11, March 23-27, 2015, Madrid, Spain

Experimental and Numerical Study of a Gas Turbine Exhaust Diffuser Applying Different Hub Extension Geometries

K. Rasouli Ghazi Kalayeh[1] *and P. Schäfer*[1]*, C. Finzel*[2] *and W. H. Hofmann*[2]

[1] German Aerospace Center, Institute of Propulsion Technology, Göttingen, Germany
keyvan.rasoulighazikalayeh@dlr.de, philipp.schaefer@dlr.de

[2] Alstom Power, Baden, Switzerland

ABSTRACT

Exhaust diffusers are utilized to recover the residual kinetic energy of the last turbine stage. The investigated diffuser consists of an annular duct and an attached Carnot diffuser. The baseline diffuser of the investigated gas turbine features a blunt end at hub, which leads to an extensive separated flow region in the Carnot diffuser. In order to reduce the separation size and the implicated losses, four different hub extension geometries and the baseline are examined numerically and experimentally for two operating conditions. The wind tunnel tests are compared to the numerical results, which are obtained by using the CFD code TRACE. Three competing performance parameters are used for analysis: pressure recovery coefficient, total pressure loss and flow uniformity factor. The investigated hub extensions lead to a reduction of the separation zones downstream of the hubs end. This results in a better diffuser performance in terms of pressure recovery coefficient and total pressure loss of all extensions compared to the baseline. As expected, the ellipsoidal extension gives the highest pressure recovery coefficient for an infinite Carnot diffuser length. At the given length of the Carnot in this case, the Hollow Cylinder lead to the best compromise for all performance parameters. In sum, the choice of the geometry depends on the available length of the Carnot diffuser and its related costs.

NOMENCLATURE

u	velocity [m/s]
C_p	pressure recovery coefficient
$C_{p,norm}$	$C_p/C_{p,baseline,A/B}$
$\widetilde{C}_{p,norm}$	$\widetilde{C}_p/C_{p,baseline,A/B}$
K	total pressure loss coefficient
K_{norm}	$K/K_{baseline,A/B}$
$\widetilde{K}_{norm}$	$\widetilde{K}/K_{baseline,A/B}$
γ	velocity uniformity factor
A	area [m^2]
L	length [m/s]
V_x	axial velocity [m/s]
p	static pressure [Pa]
p_0	total pressure [Pa]
α	swirl angle [°]
Tu	turbulence level [%]
d	diameter [m]
R_i,R_o	inner and outer radius [m]

Subscripts

a	axial direction
t	total
r	reversed flow
x	x axis
1	inlet
2	outlet
avg	average

Superscripts

—	mass flow-weighted averaged
=	area averaged
$\sim$	mixed-out

Abbreviations

DLR	German Aerospace Center
RANS	Reynolds-averaged Navier-Stokes

INTRODUCTION

Exhaust diffusers are utilized to recover the residual kinetic energy of the last turbine stage. The static pressure of the turbine's outlet is reduced, which leads to an increased pressure ratio of the turbine. Thus, the power output is increased, which generally improves the performance. Additionally, in combined cycle a heat exchanger is located downstream of the diffuser. The heat exchanger requires a uniform, low speed flow in order to work efficiently. Consequently, exhaust diffusers need to be carefully designed.

An excellent overview about the design of annular diffusers is given in the work of Japikse (1984). However, exhaust diffusers of gas turbines differ from the simple geometrical shape because of the incorporated struts. Furthermore, the investigated exhaust diffuser consists of two parts: an annular duct with two row of struts and an attached Carnot diffuser. At the transition of the two diffusing elements, the center body ends abruptly, which results in an extensive separated wake downstream in the Carnot diffuser. The blockage of this separation mitigates the adverse pressure gradient and implies undesired flow non-uniformity. Lo et al. (2012) reduced the central separation by using Coanda blowing to entrain high momentum main fluid flow towards the center. Of course, this active flow control method requires energy.

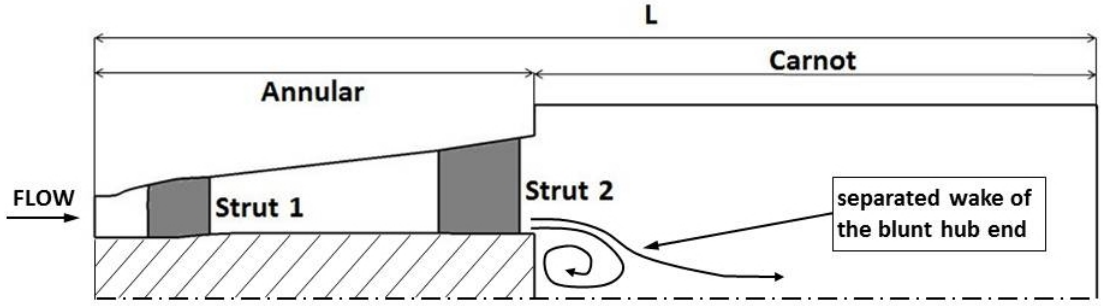

Figure 1: **Schematic of the baseline diffuser and the separated flow at the blunt hub end**

The central separation can also be reduced by shifting the onset of the adverse pressure gradient. Hirschmann et al. (2012) demonstrated by sudden expansion theory that a longer hub improves the diffuser performance. A longer hub reduces the area ratio of the expansion causing the flow to expand without separation. This leads to lower velocity at the inlet of the step diffuser and hence to a reduction in pressure loss. However, the improvement was not only dependent on the hub extension geometry, but also on the inlet boundary conditions.

An elliptical hub extension was chosen in the work of Babu et al. (2012). As a result, the elliptical configuration outperformed the baseline geometry with a blunt hub end. To overcome the manufacturing difficulties of an ellipsoid, the elliptical shape was approximated by several cylindrical hubs, which were arranged successively. However, the approximation did not shift the onset of the adverse pressure gradient, which in return led to a pressure recovery close to the baseline.

The aim of this study is to alter the onset of the adverse pressure gradient by four different hub extensions. The resulting flow structures are analyzed and compared to the baseline diffuser. Beside the geometrical shapes, two inlet conditions are applied and the flow fields are examined numerically and experimentally. Although the numerical models have been advanced in the past, the prediction of separated flow is still inaccurate using steady RANS simulations. For that reason experiments are conducted to verify the numerical results.

DEFINITIONS

Diffuser hub extensions

The baseline geometry is maintained in the annular duct as given in Figure 1. The geometry at the hub end, which is located in the Carnot diffuser, is altered by the hub extensions, which are illustrated in Figure 2. The objective of the hub extensions is to reduce the extensive separation of the blunt baseline hub. The effectiveness of the four fundamental shapes is investigated in this study and the diffuser performance parameters are introduced in the following.

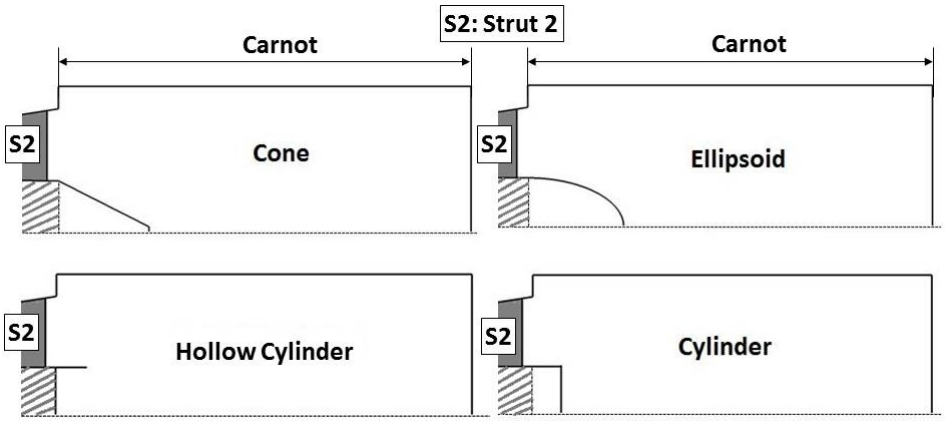

Figure 2: **Sketch of the investigated hub extensions**

Diffuser performance parameters

In order to calculate the performance parameters three types of averaging are used: the area average of the flow, the mass flow-weighted average and the values of a mixed-out flow state. The area averaged value is used for static quantities (i.e. static pressure, $\overline{p}$) and the mass averaged for total quantities such as total pressure (e.g. $\overline{\overline{p_0}}$). Both methods do not consider any entropy rise due to mixing of the non-uniform velocity flow field. The mixed-out condition of a non-uniform flow is given by the conservation mass, momentum and energy. The quantity is denoted by $\sim$ and accounts for the mixing loss, which generally leads to an increase of entropy and static pressure.

Three diffuser performance parameters are defined: the most important parameter is pressure recovery coefficient. It is given by the ratio of the static pressure increase and the dynamic pressure at the inlet of the diffuser:

$$C_p = \frac{\overline{p_2} - \overline{p_1}}{\overline{\overline{p_{01}}} - \overline{p_1}} \tag{1}$$

Total pressure loss coefficient is expressed as the ratio of the total pressure loss and the dynamic pressure at the inlet:

$$K = \frac{\overline{\overline{p_{01}}} - \overline{\overline{p_{02}}}}{\overline{\overline{p_{01}}} - \overline{p_1}} \tag{2}$$

The uniformity of the outlet velocity profile is calculated by using the ratio of area-averaged to mass flow-weighted averaged axial velocity:

$$\gamma = \frac{\overline{\tilde{u}}_a}{\overline{u}_a} \tag{3}$$

As explained by Cerantola and Birk (2012) a uniform outlet velocity profile ($\gamma = 1$) is preferable to fully expand the flow.

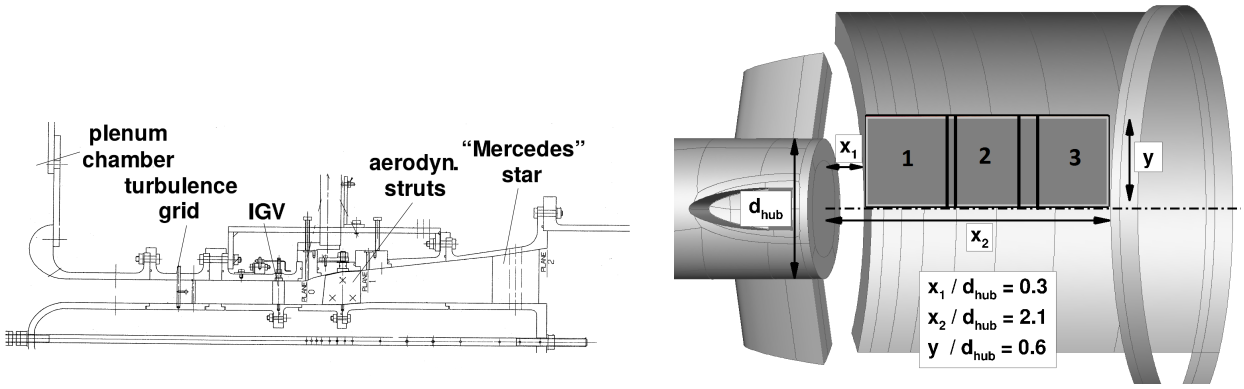

Figure 3: **The sketch of the test diffuser (left) and PIV measurement plane (right)**

EXPERIMENTAL FACILITY

The experiments were performed at the wind tunnel RGG of the German Aerospace Center Göttingen (DLR). The diffuser model of the gas turbine was obtained by a previous measurement campaign (Vassiliev et al., 2003, Vassiliev et al., 2008). In Figure 3 (left) a sketch of the diffuser model is illustrated, which consists of two main components: the inlet section and the scaled diffuser. The inlet section provides the inlet boundary conditions to the diffuser. By applying a turbulence grid and adjustable inlet guide vanes (IGV) the inflow can be altered: while the former varies turbulence intensity, the latter has been carefully designed to meet different outlet swirl distributions similar to the last turbine stage. By this, an inlet Mach number of about 0.55 is achieved, which corresponds to engine conditions. Furthermore, the Reynolds number of the diffuser model is approximately four times smaller than the full scale engine. However, it is still large enough that no Reynolds number effects are observed. An overview of the experimental setup, detailed measurement of the baseline geometry including measurement uncertainties are given by Vassiliev et al. (2003) and Schäfer et al. (2014). Based on this set-up, different hub extension were mounted and investigated by pressure taps and Particle Image Velocimetry (PIV).

PIV was applied at the hub wake in order to characterize the velocity flow field. The setup consists of a two-cavity NY:YAG laser by New Wave, a 4MP camera (PCO.2000), a smoke generator and laser light sheet optics. As illustrated in Figure 3 (right), three overlapping windows are recorded, which enable the investigation of the flow about 2.1 diameters downstream of the hub. In each window 319 pairs of two singly exposed recordings were captured and evaluated using PIVview 3.2 by PivTec GmbH. The raw images are analyzed using a $24 \times 24px^2$ interrogation window size and 50% overlap. A multiple pass, multi-grid interrogation process with a window deformation algorithm is used for the calculation of the correlation map (Scarano and Riethmuller, 1999, Scarano, 2002). The correlation peak is detected by a three-point Gaussian fit leading to sub-pixel resolution. Multiple outlier detection techniques are applied such as a maximum displacement test, vector difference test and a normalized median test to remove suspicious vectors (Westerweel and Scarano, 2005). At last, all vector fields are averaged and the three windows are merged together by linear interpolation of the overlapping regions. A slight velocity shift is observed at the overlap of the windows, which is acceptable for such a highly unsteady separated flow.

NUMERICAL SETUP

The numerical simulations are performed using the DLR in-house CFD code *TRACE*. Structured grids are obtained with *G3DHexa* with stretching ratios lower than 1.25 perpendicular to the walls and an average y^+-value of 1. The computational domain of the baseline diffuser, which consists

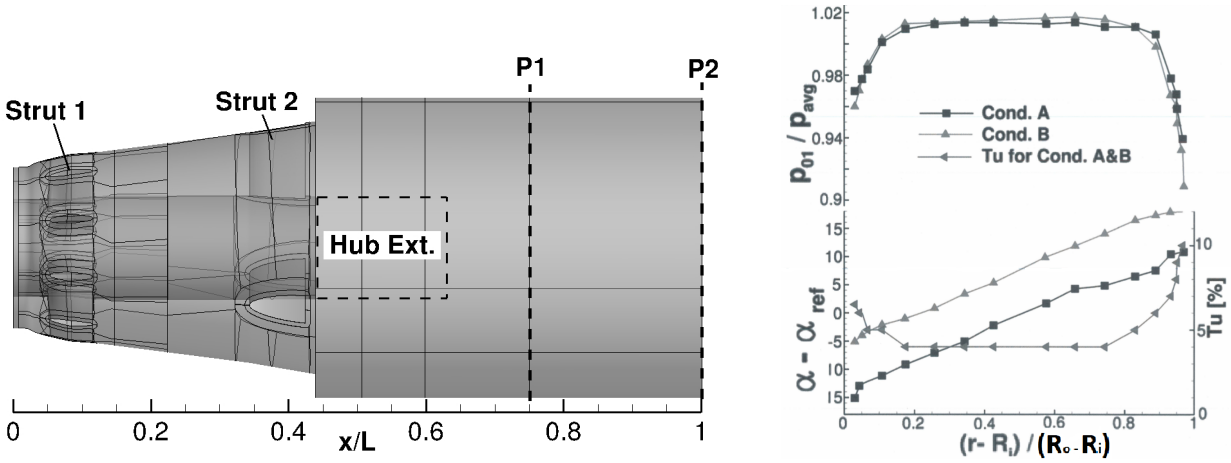

Figure 4: **The computational domain (left), inlet boundary conditions: Cond. A / B (right)**

of approximately 27 million cells, is illustrated in Figure 4 (left). As indicated, the mesh is altered according to the different hub extensions. Furthermore, two evaluation planes are introduced: Plane 1 (P1) corresponds to the experimental location of the pressure tapping and is used for the comparison of experimental and numerical data. At Plane 2 (P2) no reverse flow is observed. This enabled the correct calculation of the three performance parameters and the comparison of the numerical data. The simulations are performed in the steady state applying Menter's $k-\omega-SST$ turbulence model with a low Reynolds approach at the walls. The performance of this turbulence model in adverse pressure gradient flows gave reasonable agreements in terms of flow fields and losses (Menter, 1994, El-Behery and Hamed, 2011).

In this study, two inlet conditions denoted by Cond. A and Cond. B are investigated, which mainly differ in their radial swirl angle distribution. The radial distributions of total pressure, swirl and turbulence intensity derived from measurements are illustrated in Figure 4 (right). Thereby, the total pressure is normalized with the average total pressure at the inlet, and a reference angle, α_{ref}, which is the average swirl of Cond. A, is subtracted from the measured swirl angle. The radial swirl distributions differ by about 10 degree.

All computations achieved the following convergence criteria: massflow difference between the inlet and the outlet lower than 0.01 %, standard deviation of pressure recovery coefficient lower than 5.10^{-5} and the average and maximum norm residuals lower than the predefined upper limits.

RESULTS AND DISCUSSION

In the first two sections the experimental results are presented: pressure recovery coefficient and the corresponding velocity flow fields, which were recorded by PIV. A preliminary analysis based on the experimental data is given. Due to the limited experimental data the flow is evaluated on a numerical basis subsequently. The resulting flow fields for Cond. A and Cond. B are analyzed and the three performance parameters are discussed.

Pressure Recovery Coefficient

In Figure 5 the experimental pressure taps are compared to the circumferentially averaged wall pressure of the CFD for both conditions. Generally, a good agreement is observed for such a complex flow with a maximum difference of 5 %. Schäfer et al. (2014) showed that the main features of the flow such as total pressure distribution of the core flow and the vortical structures fit well in experimental and numerical results. Although the numerical calculations are not time resolved, the results can be used with high degree of confidence (Vassiliev et al., 2010).

Table 1: Difference of pressure recovery coefficient with the baseline evaluated at P1 (see Fig. 4)

Configuration	$\Delta C_{p,num.A}$ [-]	$\Delta C_{p,exp.A}$ [-]	$\Delta C_{p,num.B}$ [-]	$\Delta C_{p,exp.B}$ [-]
Baseline	-	-	-	-
Cone	0.004	-0.009	0.000	0.002
Ellipsoid	0.008	0.007	0.003	-0.003
Cylinder	0.009	0.004	0.005	0.003
H.-Cylinder	0.011	0.006	0.006	0.006

In Table 1 the pressure recovery coefficient difference of the experimental and numerical results with the Baseline are summarized for all extensions and both inlet conditions. For the given axial length of the Carnot diffuser the Hollow Cylinder gives the largest pressure recovery coefficient increase for both conditions. The experimental trend is predicted correctly by the numerical simulation, whereas the total difference depends on the extension and boundary condition. Generally, the absolute deviations are larger at Cond. A, where the numerical values of the Cylinders are twice as high as the corresponding experimental values. For two cases the trend is calculated incorrectly, which is the Cone at Cond. A and the Ellipsoid at Cond. B. A good agreement between the experimental and numerical value is found for the Ellipsoid. Based on the results it is inferred that the steady RANS approach is suitable for trend predictions only, whereas exact values still require experimental investigation. In sum, for both conditions an improvement is observed, whereas the overall benefit of Cond. A is pronounced compared to Cond. B.

Particle Image Velocimetry

In Figure 6 the velocity vectors with the axial velocity contours for both conditions are illustrated. The black line indicates the boundaries of separated regions. Comparing both conditions, it is realized that the mass flow moves towards the casing at Cond. A, which is due to the larger swirl angle. Because of the reduced swirl of Cond. B, the flow moves towards the center, which reduces the separation bubble. Generally, all hub extensions successfully reduced the central hub separation compared to the baseline, which was the main intention of the work.

At Cond. A all the extensions reduce the central separation region compare to the Baseline. The Ellipsoid and the Cone differ the onset of separation and the region of separation is reduced more.

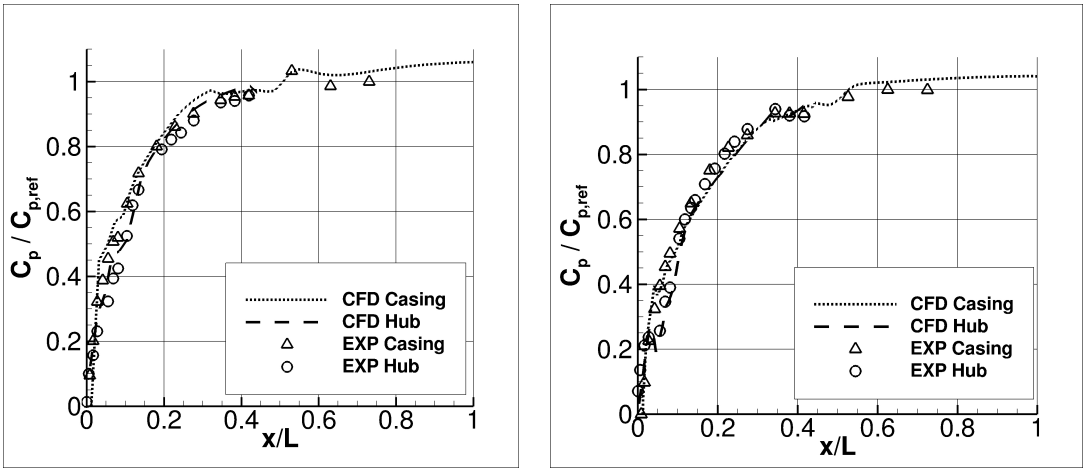

Figure 5: **Experimental and numerical pressure recovery coefficient of the baseline at Cond. A (left) and Cond. B (right)**

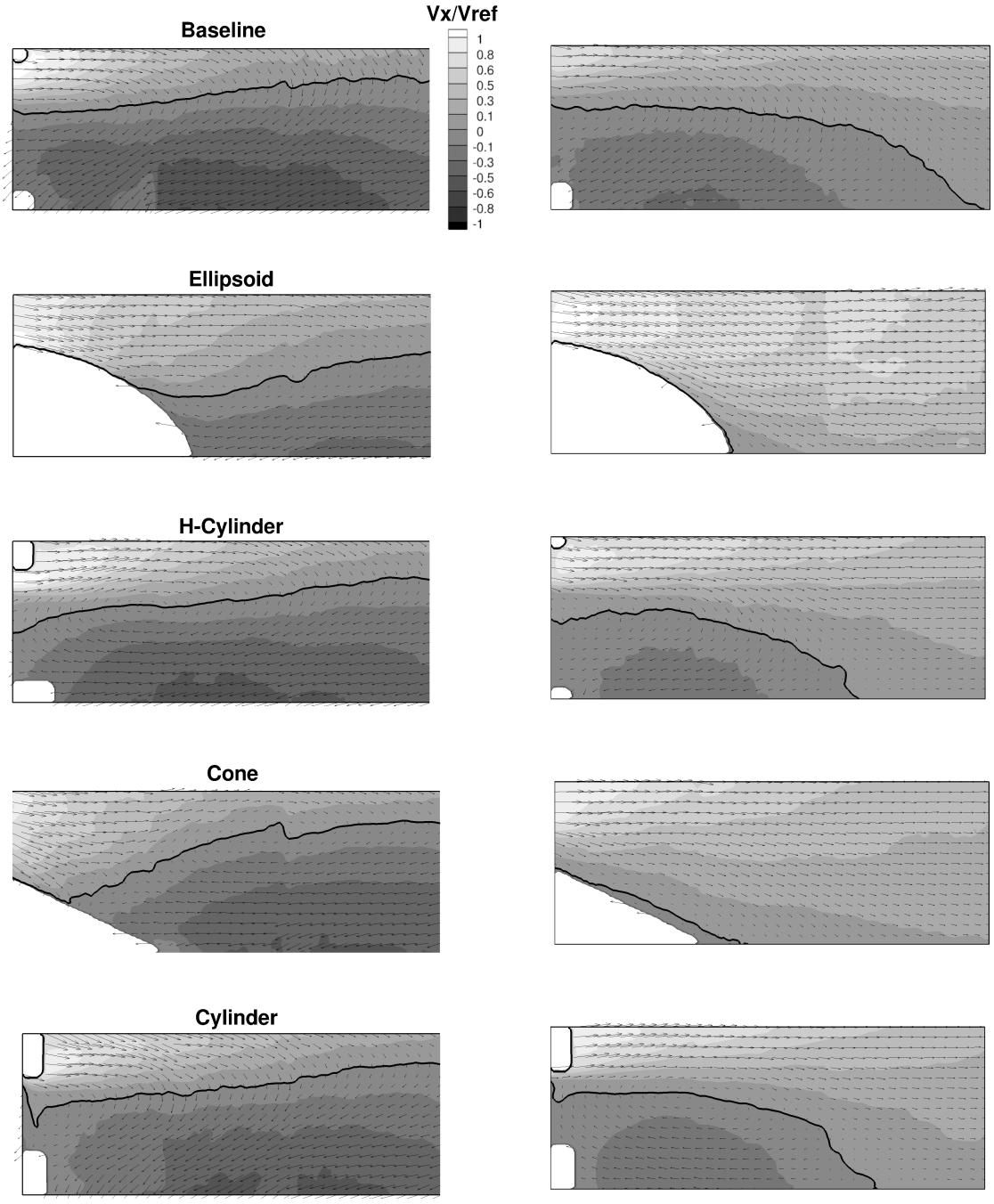

Figure 6: **PIV data: velocity vectors and normalized axial velocity contours of Cond. A (left) and Cond. B (right) along with the line of reverse flow**

Thereby, the Ellipsoid improves pressure recovery, while the Cone leads to a reduction compared to the Baseline. This is caused by moving the mass flow towards the center for the Cone, which leads to a deficit and a larger separation at the casing.

At Cond. B, the flow for the Ellipsoid is fully attached, which is recognized by the flow being shifted towards the center. Although the flow is fully attached, pressure recovery coefficient of the Ellipsoid is reduced compared to the Baseline. It is inferred that the separation at the casing must be enlarged, which would explain the reduced pressure recovery coefficient.

In conclusion, all hub extensions successfully reduced the central hub separation central separa-

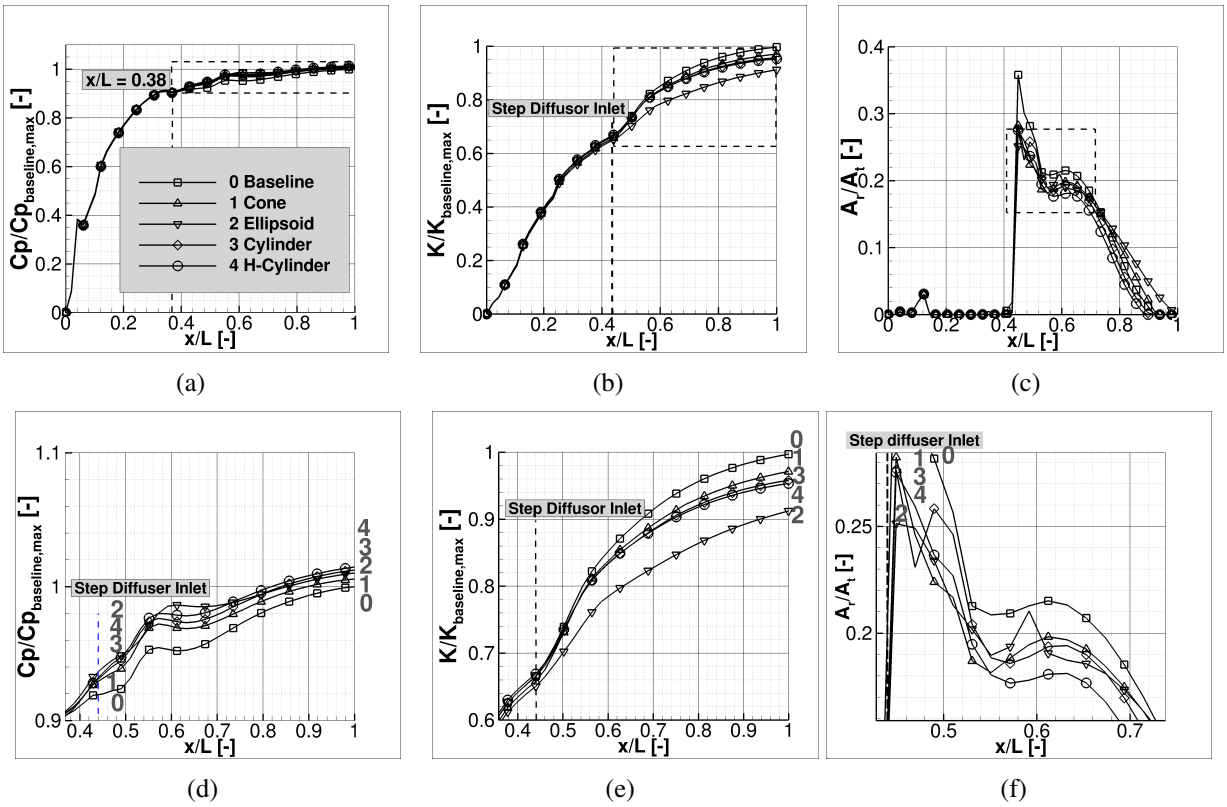

Figure 7: **Pressure recovery coefficient, total pressure loss coefficient and reversed flow area ratio of Cond. A (top) and enlargement of the hub extension region (bottom)**

tion. The reduction of the separation bubble is advantageous to some extent as it also leads to larger separation at the casing, which is, of course, undesired. Depending on the geometrical shape, the sum of the hub and the casing separation can lead to an overall reduction of pressure recovery coefficient as seen for the Ellipsiod at Cond. B. Therefore, a moderate reduction of the central separation must be achieved, which is the case for the Hollow Cylinder. Consequently, the Hollow Cylinder gives the best pressure recovery coefficient at Cond. A and Cond. B. Unfortunately, no PIV data could be recorded at the casing, so that flow fields will be analyzed based on CFD data in the following.

CFD results of Condition A

In Figure 7[a,b] pressure recovery coefficient and total pressure loss coefficient over the diffuser length are illustrated. Below of each figure, the section which contains the step diffuser is enlarged (Figure 7[d,e]). Up to $x/L = 0.38$ (close to the leading edge of Strut 2) the pressure recovery coefficient and total pressure losses of all the geometries are the same. Downstream they begin to differ from each other, especially at $x/L = 0.42$, which is the end of central hub of the baseline diffuser.

In Table 2 normalized pressure recovery coefficient, total pressure loss coefficient and velocity uniformity factor is presented. It is realized from Table 2 and Figure 7[d,e] that any hub extension improves pressure recovery coefficient and total pressure loss coefficient. The Ellipsoid has the lowest total pressure loss coefficient. The Hollow Cylinder has the largest pressure recovery coefficient and the best flow uniformity factor.

Furthermore, the velocity flow fields in the step diffuser are compared by calculating the ratio of the reverse flow area to the geometrical area. In Figure 7[c,f] the reverse flow area ratio of the diffuser and its enlarged section (dashed square in Figure 7c) are illustrated. Comparing Figure 7[d,e,f],

Table 2: Normalized performance parameters of Cond. A evaluated at P2 as given in Fig. 4

Case	Extension	$C_{p,norm}$ [-]	$\widetilde{C}_{p,norm}$ [-]	$\Delta C_{p,norm}$	K_{norm} [-]	$\widetilde{K}_{norm}$	ΔK_{norm}	γ [-]
0	-	1	1.0132	0.0132	1	1.0246	0.0246	0.848
1	Conice	1.0053	1.0198	0.0145	0.9739	0.9990	0.0251	0.831
2	Ellipsoid	1.0106	1.0304	0.0198	0.9154	0.9582	0.0428	0.768
3	Cylinder	1.0119	1.0238	0.0119	0.9607	0.9843	0.0236	0.859
4	H.-Cylinder	1.0145	1.0251	0.0106	0.9562	0.9794	0.0231	0.870

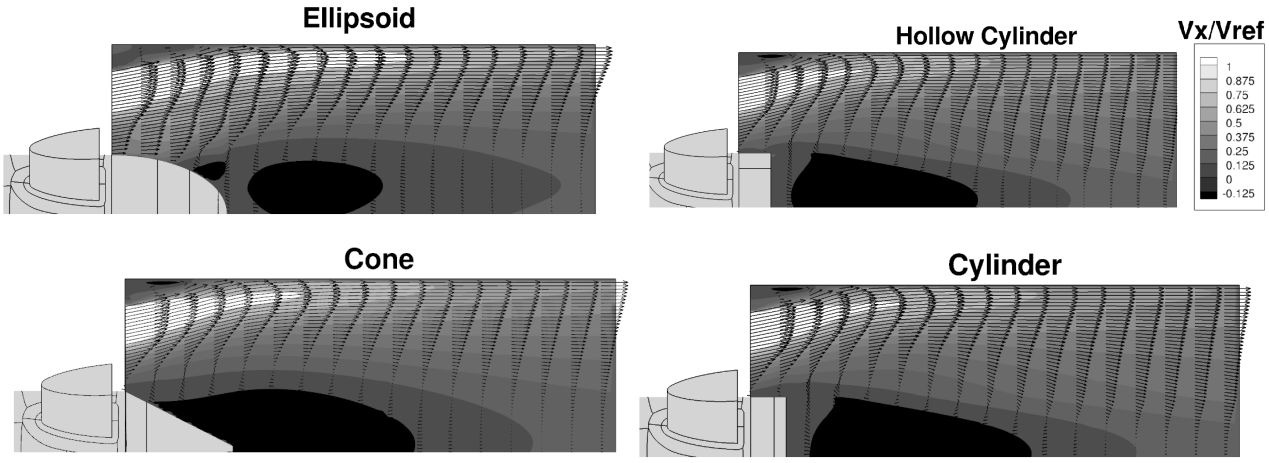

Figure 8: **Velocity vectors and normalized axial velocity contours of Cond. A**

two aspects are derived from the results: firstly, all the hub extensions delay the separation at the hub. This means that the hub extensions shift the onset of adverse pressure gradient. The delay of the separation at the hub reduces the total pressure loss (Figure 7e) due to velocity reduction at the inlet of the step diffuser, which was also found by Hirschmann et al. (2012). Secondly, Figure 7f illustrates the expansion and contraction of the core flow. Assuming an incompressible flow, which is justified by the Mach number being lower than 0.3, the ratio change in Figure 7f corresponds to the pressure recovery coefficient change in Figure 7d. Again, the Hollow Cylinder has the lowest separated area at $x/L = 0.6$, which in return gives the highest pressure recovery coefficient and the best flow uniformity factor. In this context, total pressure loss coefficient cannot be directly correlated to the two other performance parameters.

In Figure 8 axial velocity flow field is illustrated. Due to the swirl angle of the flow, the high momentum fluid is accumulated at the casing for all extensions. Comparing the flow fields in detail, it is recognized that each hub extension leads to different velocity flow field. The mixing of the shear layers of the core flow and the separation results in different separation sizes at the hub. The separation bubble of the Ellipsoid reduces at a lower rate, which leads to a delayed closure of the hub separation. Although the Ellipsoid has the lowest total pressure loss, its pressure recovery coefficient is only third best among all the geometries. This is because of the low rate of mixing and the delayed hub wake closure in the Ellipsoid step diffuser. The mixing of the flow in the Hollow Cylinder is enhanced due to circulation inwards in the hollow extension. This increased mixing moves the point of closure upstream, which gives the best flow uniformity factor at the cost of an increased pressure loss. The Cylinder behaves similar, but the closure of the hub wake is moved downstream compared to the Hollow Cylinder. The mixing is shifted downstream by the axial length of the extension, which correlates to the closure of the hub extension. As expected, the Cone gives the poorest overall flow

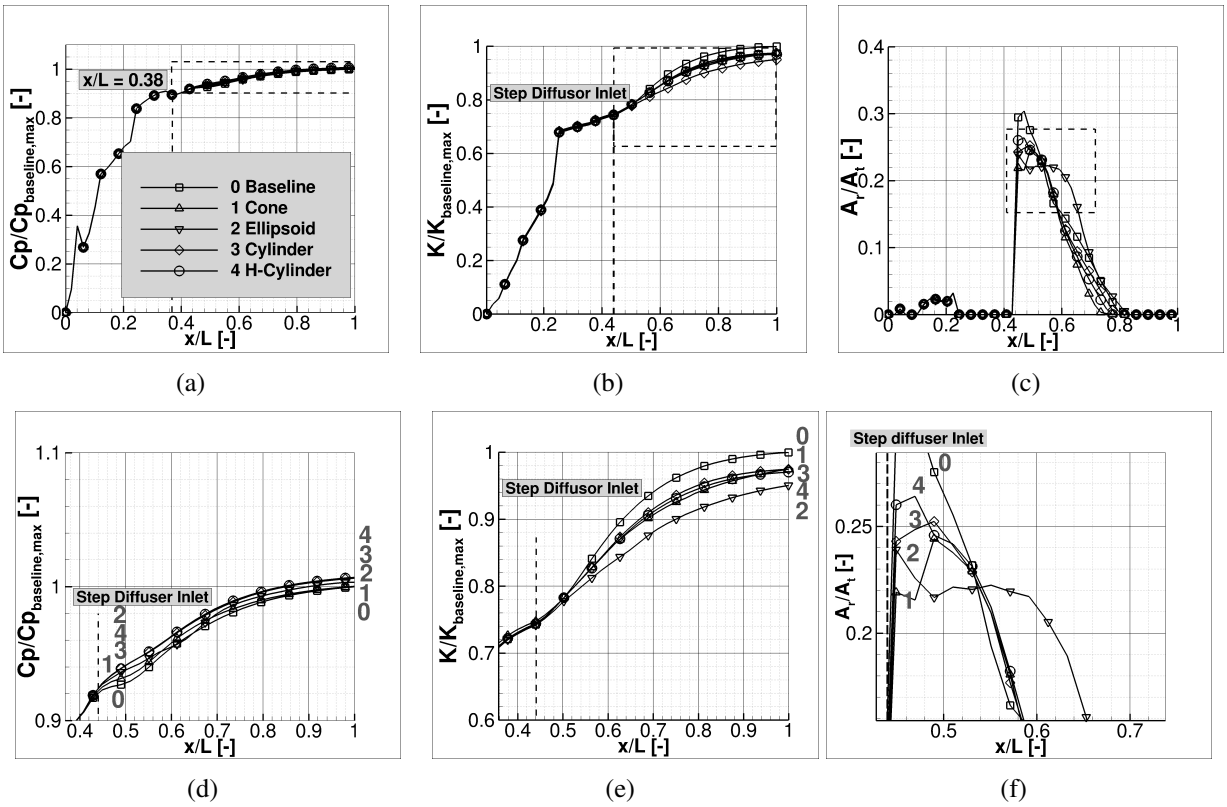

Figure 9: **Pressure recovery coefficient, total pressure loss coefficient and reversed flow area ratio of Cond. B (top) and enlargement of the hub extension region**

field.

A relationship between the pressure recovery and total pressure loss coefficient is given according to Japikse (1984) if the flow at the inlet and outlet of the diffuser is uniform, i.e. mixed-out. Therefore, the mixed-out values of performance parameters are given in Table 2 along with the differences given by the $\Delta C_{p,norm}$ and ΔK_{norm}. According to this result, the ellipsoid gives maximum pressure recovery coefficient (largest $\Delta C_{p,norm}$) while maintaining the lowest total pressure loss (largest ΔK_{norm}). However, it would require additional axial length to mix out the flow. Compared to the Hollow Cylinder, this is disadvantageous.

CFD results of Condition B

In Figure 9[a,b] pressure recovery coefficient and total pressure loss coefficient over the diffuser length are illustrated for the different hub extensions. The reverse flow area ratio of the diffuser for Cond. B and its enlarged section is given in Figure 9[c,f]. From Figure 9[f,e] it is realized that the reverse flow area is strongly reduced compared to Cond. A. This is not a benefit of the extension, but due to the reduced swirl angle, which inherently distributes the mass flow towards the center. Furthermore, the closure of the hub wake is merely influenced by the extensions except the Ellipsoid, which is different compared to Cond. A. Apart from that any hub extension improves the loss coefficient and by this pressure recovery coefficient.

A similar trend is observed in Table 3, which leads to the same conclusion: any hub extension improves pressure recovery and total pressure loss coefficient. Moreover, the Cylinder as well as the Hollow Cylinder give the best flow uniformity factor. Although the swirl angle differs compared to Cond. A, similar trends are observed: the Hollow Cylinder gives the largest pressure recovery coefficient at the costs of a slightly increased pressure recovery coefficient. Again, the Ellipsoid leads

Table 3: Normalized performance parameters of Cond. B evaluated at P2 as given in Fig. 4

Case	Extension	$C_{p,norm}$ [-]	$\widetilde{C}_{p,norm}$ [-]	$\Delta C_{p,norm}$	K_{norm} [-]	$\widetilde{K}_{norm}$	ΔK_{norm}	γ [-]
0	-	1	1.0045	0.0045	1	1.0102	0.0102	0.8967
1	Cone	1.0003	1.0065	0.0062	0.9748	1.0049	0.0301	0.9057
2	Ellipsoid	1.0043	1.0114	0.0071	0.9503	0.9806	0.0303	0.8807
3	Cylinder	1.0064	1.0107	0.0043	0.9746	0.9843	0.0097	0.9457
4	H.-Cylinder	1.0069	1.0116	0.0047	0.9703	0.9806	0.0103	0.9412

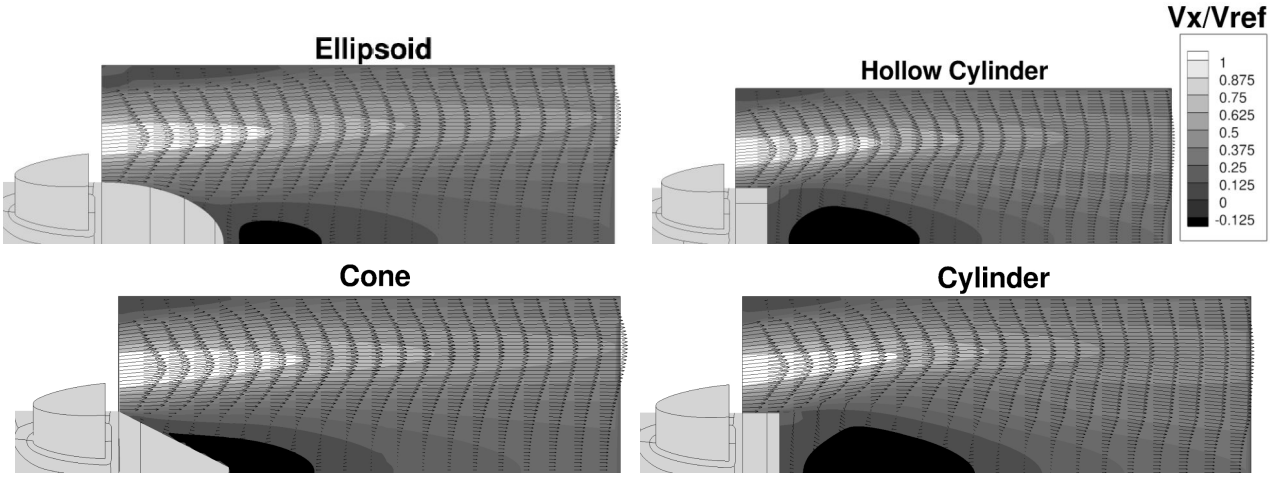

Figure 10: **Velocity vectors and normalized axial velocity contours of Cond. B**

to lowest total pressure loss coefficient with a reduced pressure recovery coefficient. The mixed-out values of the Ellipsoid give the maximum pressure recovery coefficient along with the lowest total pressure loss, which would require additional axial length compared to the Hollow Cylinder. In sum, the benefit of all hub extensions is reduced by a factor of about two due to the reduced swirl angle.

In Figure 10 the velocity fields are illustrated. All hub extensions leads to a similar flow pattern with only little difference. Compared to Cond. A, the separated area at the casing is larger for all extensions. By this, the separation at the hub is reduced inherently by the flow and is merely dependent on the configuration. In sum, the flow field is in line with the overall smaller improvements of the performance parameters at Cond. B.

CONCLUSION

The impact of four different hub extensions on the performance of a typical exhaust diffuser is presented in this paper. The Baseline diffuser geometry is modified by different endings at the hub including a Cylinder, a Hollow Cylinder, an Ellipsoid and a Cone. Their performance is numerically assessed using three competing performance parameters. Two different inlet boundary conditions are considered, of which Cond. A has an increased swirl angle compared to Cond. B. The numerical results are compared to experimental data from the diffuser test rig.

According to the numerical and experimental results each hub extension improves the pressure recovery coefficient, except for the Cone at Cond. A and the Ellipsoid at Cond. B. The general trend is picked up correctly by the numerical simulation, whereas the absolute difference depends on the extension and the boundary condition. While the experimental and numerical data agree reasonably well for Cond. B, a larger deviation is observed for Cond. A. The difference is explained by the steady RANS approach and the incapability of predicting the large separated hub wake correctly.

At Cond. A the Hollow Cylinder leads to the largest pressure recovery coefficient. Although its pressure loss coefficient is slightly larger than the Ellipsoid, it is outperforming the other configurations. Furthermore, the Hollow Cylinder gives the best flow uniformity factor. Consequently, the Hollow Cylinder provides the best performance factors at the given length compared to the other configurations.

At Cond. B the improvements of all hub extensions are reduced compared to Cond. A. This is due to reduced inlet swirl, which leads to a pronounced separation at the Carnot casing. Thus, the separation at the hub end is reduced inherently by the flow and is not as dependent on the configuration as in Cond. A. At Cond. B the Hollow Cylinder outperforms all the other hub extensions over the complete axial length.

The Hollow Cylinder is the best extension based on the experimental and numerical investigation at the two boundary conditions. Further numerical investigations should include a variation of the hub extension parameters, for example, the axial length or the cone angle, additional operating conditions as well as time resolving simulation.

Acknowledgement

The investigations were conducted as part of the joint research program COORETEC-turbo (AG Turbo 2020) in the frame of AG Turbo. The work was supported by the Bundesministerium für Wirtschaft und Technologie (BMWi) as per resolution of the German Federal Parliament under grant number 0327718D. The authors gratefully acknowledge AG Turbo and Alstom for their support and permission to publish this paper. The responsibility for the content lies solely with its authors.

REFERENCES

Babu, M. and Shukla, R. K. and Maru, A. and Pradeep, A. M. and Roy, B., 2012. *Boundary Layer Control in Turbine Exhaust Diffusers Using Casing Injection and Design Modifications.* ASME Turbo Expo, Conference Proceeding

Cerantola, David J. and Birk, A. M., 2012. *Numerically optimizing an annular diffuser using a genetic algorithm with three objectives.* ASME Turbo Expo, Conference Proceeding

El-Behery, S. M., and Hamed, M. H., 2011. *A comparative study of turbulence models performance for separating flow in a planar asymmetric diffuser.* Computers and Fluids, pp. 248-257.

Hirschmann, A., Volkmer, S., Casey, M., Montgomery M., 2012. *Hub extension in an axial gas turbine diffuser.* ASME Turbo Expo, Conference Proceeding

Japikse L., D., 1984. *Diffuser Design Technology.* Concepts ETI, Inc. Norwich.

Lo, K. P., Elkins, C. J. and Eaton, J. K. 2012. *Separation control in a conical diffuser with an annular inlet: center body wake separation.* Exp Fluids 53:1317-1326

Klein, A., 1981. *Effects of inlet conditions on conical-diffuser performance.* J. Fluid Eng., 103, pp. 250-257.

Menter, F. R., 1994. *Two-equation eddy-viscosity turbulence models for engineering applications.* AIAA Journal, Vol. 32, No. 8

Schäfer, P., Gieß P.-A., Finzel, C. and Hofmann, W. H., 2014. *Impact of inlet endwall blockage on the performance of exhaust diffuser geometry of heavy duty gas turbines.* ASME Turbo Expo, Conference Proceeding

Schetz, J. A. and Fuhs, A. E. 1996. *Handbook of Fluid Dynamics and Fluid Machinery.* WILEY-Interscience.

Stevens, S. J., and Williams, G. J., 1980. *The influence of inlet conditions on the performance of annular diffusers.* J. Fluid Eng., 102, pp. 357-363.

Sovran, G., and Klomp, E., 1967. *Experimentally determined optimum geometries for rectilinear diffusers with rectangular, conical or annular cross-section.* Mechanics of Internal Flow, Elsevier.

Scarano, F. and Riethmuller, ML, 1999. *Iterative multigrid approach in PIV image processing with discrete window offset.* J. Experiments in Fluids, Springer, Vol. 26, pp. 513-523.

Scarano, F, 2002. *Iterative image deformation methods in PIV.* J. Measurement Science and Technology, IOP Publishing, Vol. 13

Vassiliev, V., Irmisch, S., Abdel-Wahab, S., and Granovskiy, A., 2010. *Impact of the inflow conditions on heavy-duty gas turbine exhaust diffusers performance.* ASME Turbo Expo, Conference Proceeding

Vassiliev, V., Irmisch, S., Claridge, M., and Richardson, D.,2003. *Experimental and numerical investigation of the impact of swirl on the performance of industrial gas turbines exhaust diffusers.* ASME Turbo Expo, Conference Proceeding

Vassiliev, V., Rothbrust, M., and Irmisch, S., 2008. *Refitting of exhaust diffuser of industrial gas turbine.* ASME Turbo Expo, Conference Proceeding

Westerweel, J. and Scarano, F. 2005. *Universal outlier detection for PIV data* J. Experiments in Fluids, Springer, Vol. 39, pp. 1096-1100.